3-D numerical simulation of Yb:YAG active slabs with longitudinal doping gradient for thermal load effects assessment

P. Ferrara,[1] M. Ciofini,[2] L. Esposito,[3] J. Hostaša,[3,4] L. Labate,[1,5,*] A. Lapucci,[2] A. Pirri,[6] G. Toci,[6] M. Vannini,[6] and L. A. Gizzi[1,5]

[1]Istituto Nazionale di Ottica, Consiglio Nazionale delle Ricerche, Via G. Moruzzi, 1 - I-56124 Pisa, Italy
[2]Istituto Nazionale di Ottica, Consiglio Nazionale delle Ricerche, Largo Enrico Fermi 6, I-50125 Firenze, Italy
[3]Istituto di Scienza e Tecnologia dei Materiali Ceramici, Consiglio Nazionale delle Ricerche, Via Granarolo 64, 48018 Faenza, Italy
[4]Department of Glass and Ceramics, ICT Prague, Technická 5, 166 28 Prague, Czech Republic
[5]Istituto Nazionale di Fisica Nucleare, Sezione di Pisa and Laboratori Nazionali di Frascati, Italy
[6]Istituto Nazionale di Ottica, Consiglio Nazionale delle Ricerche, Via Madonna del Piano 10, I-50019 Sesto Fiorentino (FI), Italy
[*]luca.labate@ino.it

Abstract: We present a study of Yb:YAG active media slabs, based on a ceramic layered structure with different doping levels. We developed a procedure allowing 3D numerical analysis of the slab optical properties as a consequence of the thermal load induced by the pump process. The simulations are compared with a set of experimental results in order to validate the procedure. These structured ceramics appear promising in appropriate geometrical configurations, and thus are intended to be applied in the construction of High Energy Diode Pumped Solid State Laser (DPSSL) systems working in high repetition-rate pulsed regimes.

OCIS codes: (140.0140) Lasers and laser optics; (140.3580) Lasers, solid-state; (140.3480) Lasers, diode-pumped; (140.6810) Thermal effects; (140.3615) Lasers, ytterbium.

References and links

1. W. Koechner, *Solid-State Laser Engineering*, 2nd ed. (Springer, 1988).
2. A. Cousins, "Temperature and thermal stress scaling in finite-length end-pumped laser rods," IEEE J. Quantum Electron. **28**(4), 1057–1069 (1992).
3. S. C. Tidwell, J. F. Seamans, and M. S. Bowers, "Highly efficient 60-W TEM_{00} cw diode-end-pumped Nd:YAG laser," Opt. Lett. **18**(2), 116–118 (1993).
4. X. Yan, Q. Liu, L. Huang, Y. Wang, X. Huang, D. Wang, and M. Gong, "A high efficient one-end-pumped TEM_{00} laser with optimal pump mode," Laser Phys. Lett. **5**(3), 185–188 (2008).
5. W. F. Krupke, "Ytterbium solid-state lasers—the first decade," IEEE J. Sel. Top. Quantum Electron. **6**(6), 1287–1296 (2000).
6. M. Siebold, J. Hein, C. Wandt, S. Klingebiel, F. Krausz, and S. Karsch, "High-energy, diode-pumped, nanosecond Yb:YAG MOPA system," Opt. Express **16**(6), 3674–3679 (2008).
7. S. Basu and R. L. Byer, "Average power limits of diode-laser-pumped solid state lasers," Appl. Opt. **29**(12), 1765–1771 (1990).
8. A. Giesen, H. Hügel, A. Voss, K. Wittig, U. Brauch, and H. Opower, "Scalable concept for diode-pumped high-power solid-state lasers," Appl. Phys. B **58**(5), 365–372 (1994).
9. J. Lu, M. Prabhu, K. Ueda, H. Yagi, T. Yanagitani, and A. Kudryashov, "Highly efficient lasers using polycrystalline Nd:YAG ceramics," Proc. SPIE **4184**, 373–376 (2001).
10. J. Lu, K. Ueda, H. Yagi, T. Yanagitani, Y. Akiyama, and A. A. Kamiskii, "Neodymium doped yttrium aluminum garnet (Y_3 Al_5 O_{12}) nanocrystalline ceramics—a new generation of solid state laser and optical materials," J. Alloy. Comp. **341**(1-2), 220–225 (2002).
11. J. Lu, H. Yagi, K. Takaichi, T. Uematsu, J.-F. Bisson, Y. Feng, A. Shirakawa, K.-I. Ueda, T. Yanagitani, and A. A. Kaminskii, "110 W ceramic Nd:Y_3 Al_5 O_{12} laser," Appl. Phys. B **79**(1), 25–28 (2004).
12. I. Shoji, S. Kurimura, Y. Sato, T. Taira, A. Ikesue, and K. Yoshida, "Optical properties and laser characteristics of highly Nd^{3+}-doped Y_3 Al_5 O_{12} ceramics," Appl. Phys. Lett. **77**(7), 939–941 (2000).
13. A. Pirri, D. Alderighi, G. Toci, and M. Vannini, "High-efficiency, high-power and low threshold Yb3+:YAG ceramic laser," Opt. Express **17**(25), 23344–23349 (2009).

#202559 - $15.00 USD Received 4 Dec 2013; accepted 27 Jan 2014; published 28 Feb 2014

14. A. Lapucci, M. Ciofini, M. Vannoni, and A. Sordini, "High efficiency, diode pumped Nd:YAG ceramics slab laser with 230 W continuous-wave output power," Appl. Opt. **51**(18), 4224–4231 (2012).
15. N. Vretenar, T. Carson, A. Lobad, P. Peterson, T. C. Newell, and W. P. Latham, "Thermal management investigations in ceramic thin disk lasers," Proc. SPIE **7836**, 78360J1 (2010).
16. D. Kracht, R. Wilhelm, M. Frede, K. Dupré, and L. Ackermann, "407 W end-pumped multi-segmented Nd:YAG laser," Opt. Express **13**(25), 10140–10144 (2005).
17. T. Kamimura, T. Okamoto, Y. L. Aung, and A. Ikesue, "Ceramic YAG composite with Nd gradient structure for homogeneous absorption of pump power," in *Conference on Lasers and Electro-Optics (CLEO)* OSA Technical Digest Series (CD) (2007), paper CThT6.
18. Y. Sato, A. Ikesue, and T. Taira, "Tailored spectral designing of layer-by-layer type composite Nd:Y3ScAl4O12/Nd:Y3Al5O12 ceramics," IEEE J. Sel. Top. Quantum Electron. **13**(3), 838–843 (2007).
19. F. Tang, Y. G. Cao, J. Q. Huang, W. Guo, H. G. Liu, W. C. Wang, Q. F. Huang, and J. T. Li, "Diode-pumped multilayer Yb:YAG composite ceramic laser," Laser Phys. Lett. **9**(8), 564–569 (2012).
20. L. Esposito, T. Epicier, M. Serantoni, A. Piancastelli, D. Alderighi, A. Pirri, G. Toci, M. Vannini, S. Anghel, and G. Boulon, "Integrated analysis of non-linear loss mechanisms in Yb:YAG ceramics for laser applications," J. Eur. Ceram. Soc. **32**(10), 2273–2281 (2012).
21. W. Koechner, "Transient thermal profiles in optically pumped laser rods," J. Appl. Phys. **44**(7), 3162–3170 (1973).
22. W. Koechner and D. K. Rice, "Effect of birefringence on the performance of linearly polarized YAG: Nd lasers," IEEE J. Quantum Electron. **6**(9), 557–566 (1970).
23. S. Chénais, F. Druon, S. Forget, F. Balembois, and P. Georges, "On thermal effects in solid-state lasers: The case of ytterbium-doped materials," Prog. Quantum Electron. **30**(4), 89–153 (2006).
24. A. Lapucci, M. Ciofini, L. Esposito, P. Ferrara, L. A. Gizzi, J. Hostaša, L. Labate, A. Pirri, G. Toci, and M. Vannini, "Characterization of Yb:YAG active slab media based on a layered structure with different doping," Proc. SPIE **8780**, 87800J1 (2013).
25. COSMOS M, Design Star Product, Structural Research and Analysis Corp. – (User's Guide and Tutorial), www.cosmosm.com, Los Angeles (2001).
26. G. Toci, M. Ciofini, L. Esposito, P. Ferrara, L. A. Gizzi, J. Hostaša, L. Labate, A. Lapucci, A. Pirri, and M. Vannini are preparing a manuscript to be called "Experimental measurement of the thermal lens effect and birefringence in Yb:YAG ceramics with layered structure."
27. A. Lucianetti, D. Albach, and J.-C. Chanteloup, "Active-mirror-laser-amplifier thermal management with tunable helium pressure at cryogenic temperatures," Opt. Express **19**(13), 12766–12780 (2011).
28. M. Azrakantsyan, D. Albach, N. Ananyan, V. Gevorgyan, and J.-C. Chanteloup, "Yb^{3+}:YAG crystal growth with controlled doping distribution," Opt. Mater. Express **2**(1), 20–30 (2012).
29. R. Paschotta, *Encyclopedia of Laser Physics and Technology* (John Wiley, 2008).
30. M. Born and E. Wolf, *Principles of Optics – Electromagnetic Theory of Propagation, Interference and Diffraction of Light*, 7th ed. (Cambridge University, 1999).
31. E. A. Khazanov, "Thermally induced birefringence in Nd:YAG ceramics," Opt. Lett. **27**(9), 716–718 (2002).
32. I. Shoji, Y. Sato, S. Kurimura, V. Lupei, T. Taira, A. Ikesue, and K. Yoshida, "Thermal-birefringence-induced depolarization in Nd:YAG ceramics," Opt. Lett. **27**(4), 234–236 (2002).

1. Introduction

In Diode-Pumped Solid State Lasers (DPSSLs) with end-pumped geometry, excellent efficiencies can be obtained along with a good modal selection, due to the optimal spatial matching of the pumping beam with the fundamental mode of the laser resonator [1,2]. In such geometries, power extraction is ultimately limited by consistent thermal distortions arising in the active medium even for relatively small pumping powers [3]. Thermal distortions of the active medium produce deleterious effects such as thermal lensing, depolarization and bifocusing. Thus, carefully optimized designs are needed to combine the high laser efficiency with maximum power extraction capabilities [4]. The impact of pump heating is considerably reduced choosing a gain medium with a favourable energy level structure, such as ytterbium-doped materials [1,5]. In Yb:YAG active medium the quantum defect is small (less than 10%). Moreover, the absence of energy levels other than those concerned with pump and laser radiation, prevents the occurrence of parasitic processes (excited-state absorption, up-conversion, self quenching), making thermal load further reduced. Yb:YAG is also an optimal candidate for the attainment of High Energy DPSSLs working in high repetition rate pulsed regimes [6] thanks to its relatively long upper state lifetime. However, owing to the quasi-three-level scheme, high pumping intensities are required to deplete the ground state population.

#202559 - $15.00 USD Received 4 Dec 2013; accepted 27 Jan 2014; published 28 Feb 2014

Specific architectures, such as the slab laser [7] or the disk laser [8], have been adopted in the past to overcome the limits imposed by thermal distortions of the active medium.

Recently, ceramics have been produced and tested in laser systems [9–11]. Good mechanical properties, more uniform composition, shorter production time, larger slabs size, superior micro-hardness and fracture toughness, together with higher doping concentration of laser active ions, have been demonstrated [12,13]. Nd:YAG and Yb:YAG ceramics have been successfully employed in high power lasers, with slab or disk geometry [14,15]. Most importantly, ceramic materials present the further advantage of allowing an easy production of composite structures with different doping levels. These structured active media have been proposed [16–18] as a possible solution to the thermal problem. Multi-layer active media can be produced with a combination of tape casting and hot-isostatic pressing (HIP) technology. The biggest drawback of HIP method is the high fabrication cost that it implies. Recently, it has been found that simple vacuum sintering technology with optimized fabrication parameters can be used in place of HIP, which can significantly limit the production costs [19,20].

Thermal effects in solid state lasers have been widely investigated from the theoretical point of view. The early works by Koechner [21,22] were devoted to address thermal effects in laser rods. The modelling was done in a two-dimensional approximation, either with the idealization of an infinitely long laser rod subject to uniform pumping, or utilizing the approximations of two-dimensional temperature variations. A thorough review of the studies on diode-pumped lasers with special reference to ytterbium-doped materials has been presented in a recent paper [23]. In this work the authors provide an interesting discussion about the main approximations adopted for modelling thermal effects in end-pumped lasers, namely, the plain strain approximation (long rods) and the plain stress approximation (thin discs). In both cases the three dimensional problem can be reduced to a two dimensional one, either for translational invariance (plain strain) or for small longitudinal variations (plain stress).

A non-uniform doping distribution leads to an absence of any translational symmetry, and thus quests for a full three-dimensional model. In our work, we adopt a numerical approach based on Finite Element Mesh (FEM) analysis, allowing a longitudinal variation of the parameters. This enables us to estimate thermal distributions and thermo-mechanical stresses in spatially structured active media. The calculation of optical wavefront aberrations generated inside the distorted active media permits to evaluate their different behaviours in terms of thermal lens. The work is aimed at optimizing the longitudinal doping profile in a ceramic Yb:YAG specimen. Experimental measurements of thermal lens effective focal lengths (EFLs) are used to validate our numerical approach. We also show that optimal doping distribution is strongly related to the pumping and cooling geometry. This complex numerical analysis is necessary in order to assess the advantages or disadvantages of a specific doping distribution design in terms of thermal effects.

In this paper we report on the thermal effects analysis on structured samples referring to a cooling and pumping geometry available in our lab [24]. Consistently with the experimental observations our simulations show that a longitudinal variation of the Yb doping does not produce significant advantages in terms of thermal effects. This appears to be true as long as the cooling direction is substantially transverse. For comparison we show some results in case of a longitudinal cooling geometry, typical of active-mirror or disk lasers. In this case longitudinally structured samples do show advantages in terms of thermal lens reduction. This result appears more relevant for systems with a high aspect-ratio (d/t), that is the ratio between the pumped volume diameter (d) and the sample thickness (t).

#202559 - $15.00 USD Received 4 Dec 2013; accepted 27 Jan 2014; published 28 Feb 2014

2. Description of the simulation model

2.1 FEM model

In this subsection the methodology is described, adopted to provide a numerical solution to the thermo-mechanical problem of a laser irradiated slab with longitudinal doping gradient.

The Finite Element Method (FEM) software COSMOS, which provides a powerful numerical solver [25], has been used to perform this analysis.

The simulated slabs have all a cylindrical shape with a 10 mm diameter and 3 mm thickness. They are pumped on a 0.5 mm diameter region on one side. As it will be discussed later, we simulated 2 different cooling geometries: in the first one the slab is cooled on a ring surface external to a 5 mm diameter on the opposite side with respect to the pump, see Fig. 1(a); in the second one the cooling is applied to the whole surface, see Fig. 1(b). The first cooling geometry exactly models our experimental test bed [24–26] and is used for the model validation. The second cooling scheme models the one-sided face-cooling characterizing *disk* or *active-mirror* lasers [27]. To compare the results in the two different situations we have always modelled the pumping as a single passage pump-beam scheme.

The typical computational grid is shown in Fig. 1(c). The central region shows a finer mesh which corresponds to the pumped region. The outer region, where a coarser mesh is used, is where the heat flows through the slab away from the pumped volume.

Each slab is modelled as a stack of 5 equally thick layers, each layer having its own doping. Different combinations of the 5 layer dopings were simulated, thus corresponding to different longitudinal absorption profiles. In order to perform a significant comparison, the incident pump power is adjusted so as to obtain the same optical absorption in each sample. Such absorption was set to 25 W, which, in the specific case of Yb:YAG, corresponds to a total thermal load (*i.e.* the power to be dissipated) of about 2.6 W.

The pump absorption in each layer was calculated using the absorption coefficient $\alpha = A \cdot \delta_{\%}$, where $\delta_{\%}$ is the Ytterbium doping percentage in the chosen layer and A = 0.5 cm^{-1} [28,29].

Each layer is heated with a power density that can be calculated as the power absorbed by the single layer divided by its volume. On the surface in contact with copper heat sink the temperature is set to T_{REF} = 20°C; the initial condition for the simulation is T_{IN} = 20°C in the whole slab.

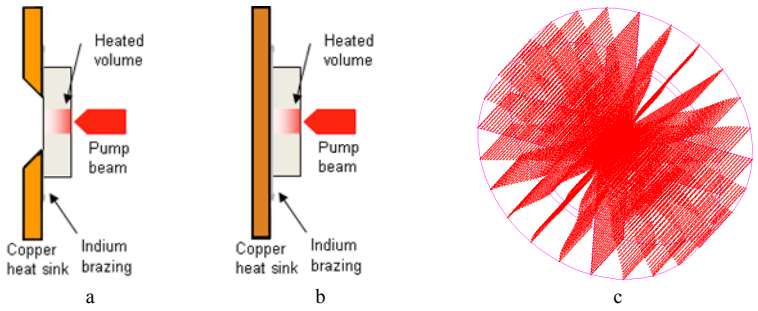

Fig. 1. Pictorial view of the simulated geometries with COSMOS software package. (**a**): annular cooling; (**b**): cooling on the whole surface; (**c**): finite element grid of the computational domain.

2.2 Calculation of induced wavefront aberrations

In a slab active medium, the induced optical path difference *OPD(r)* at different transverse positions with respect to an unperturbed beam is related to 3 contributions [22,23]:

#202559 - $15.00 USD Received 4 Dec 2013; accepted 27 Jan 2014; published 28 Feb 2014

• the surface bulging due to thermal expansion,

• the refractive index variations with temperature,

• the stress induced birefringence due to the photo-elastic effect.

Hence *OPD(r)* can be calculated by using this formula (we assume here a cylindrical symmetry):

$$OPD(r) = (n_0 - 1)\cdot \Delta L(r) + \int_0^{L+\Delta L(r)} \left(\frac{\partial n}{\partial T}\right)_{\varepsilon} \cdot \left(T(r) - T_{REF}\right) dz + \sum_{j=r,\vartheta,z} \left(\int_0^{L+\Delta L(r)} \left(\frac{\partial n}{\partial \varepsilon_j}\right)_T \cdot \varepsilon_j(r)\, dz \right) \tag{1}$$

where L is the slab thickness without pumping, n_0 is the refractive index without deformations ($n_0 = 1.82$ for Yb:YAG), T_{REF} is the temperature of the cooling system ($T_{REF} = 20°C$), *ΔL(r)* is the surface deformation at radial position r , ε_j is a diagonal component of the strain tensor, and z is the direction parallel to the cylindrical axis. Variables *(r, θ)* refer to the polar coordinate system in the plane transverse to propagation.

The FEM thermo-mechanical analysis described in the previous sub-section provides a group of data for each node of the computational grid:

• a scalar temperature variation field $\Delta T = \left(T - T_{REF}\right)$,

• the 3 components of the displacements,

• the 6 components of the stress tensor (3 for σ_i and 3 for τ_{ij}) [23].

Strains (ε_{ij}) can be easily calculated from the stress and temperature fields using the conventional constitutive equations for linear elastic deformations in a material:

$$\begin{cases} \varepsilon_r = \frac{1}{E}\left[\sigma_r - \nu\left(\sigma_\phi + \sigma_z\right)\right] + \alpha\left(T - T_{REF}\right) \\ \varepsilon_\phi = \frac{1}{E}\left[\sigma_\phi - \nu\left(\sigma_r + \sigma_z\right)\right] + \alpha\left(T - T_{REF}\right); \\ \varepsilon_z = \frac{1}{E}\left[\sigma_z - \nu\left(\sigma_\phi + \sigma_r\right)\right] + \alpha\left(T - T_{REF}\right) \end{cases} \tag{2}$$

$$\begin{cases} \varepsilon_{r\phi} = \left(\frac{1+\nu}{E}\right)\tau_{r\phi} \\ \varepsilon_{rz} = \left(\frac{1+\nu}{E}\right)\tau_{rz}; \\ \varepsilon_{\phi z} = \left(\frac{1+\nu}{E}\right)\tau_{\phi z} \end{cases} \tag{3}$$

where, considering our host material (YAG), $E = 2.8\cdot 10^{11} Pa$ is the Young modulus, $\nu = 0.28$ is the Poisson coefficient, $\alpha = 7.9\cdot 10^{-6} / K$ is the thermal expansion coefficient.

The first two contributions to the OPD (thermal and surface contribution) can be directly calculated from the output of the thermo-mechanical simulations. To determine the third contribution we need the relation between the refractive index (for a non-polarized beam) and the strain tensor. This relation is in general expressed by a variation of the dielectric impermeability 2nd rank tensor B_{ij} as a function of strains [22], (B_{ij} is defined as the reciprocal of the permeability 2nd rank tensor [30]). We thus can write:

#202559 - $15.00 USD Received 4 Dec 2013; accepted 27 Jan 2014; published 28 Feb 2014

$$\Delta B_{ij} = p_{ijkl}\varepsilon_{kl}, \tag{4}$$

where p_{ijkl} is the 4th rank elasto-optical tensor. Equation (4) is valid only in a coordinate system with the axes parallel to the crystal axes (for the sake of simplicity, we will call this system "crystal oriented coordinate system"). The components of the impermeability 2nd rank tensor (B_{ij}) are the coefficients of an ellipsoid, called "indicatrix", that, in the principal directions (indicated with the " ~ " symbol), can be expressed by this formula:

$$\sum_{i=1,2,3}\left(\widetilde{B}_i x_i^2\right) = 1, \tag{5}$$

where:

$$\widetilde{B}_i = \left(B_0 + \Delta\widetilde{B}_i\right) = \frac{1}{n_i^2}, \tag{6}$$

for a diagonal dielectric impermeability tensor. The index of refraction can be written as:

$$n_i = n_0 + \sum_{j=r,\vartheta,z}\left(\left(\frac{\partial n_i}{\partial \varepsilon_j}\right)_T \cdot \varepsilon_j(r)\right), \tag{7}$$

where: n_i is the refractive index along one of the principal directions of the stress-perturbed indicatrix [22], $\widetilde{B}_i$ is the dielectric impermeability tensor along one of the principal directions, B_0 is the initial value of this tensor in such directions: $\left(B_{IN}\right)_{ij} = B_0\delta_{ij}$, where: $B_0 = \frac{1}{n_0^2} \simeq 0.30$.

Equation (4), involving the 4th rank tensor, reduces to a much simpler formulation in the case of a cubic crystal with [111] orientation [22,23]. Moreover Khazanov *et al.* [31] demonstrated that the YAG ceramic behaviour is similar to that of the [111] oriented single crystal, given the averaging effect of the different grains orientations. This fact was also confirmed by experimental birefringence measurements in Nd:YAG ceramics [32]. Under these conditions the impermeability tensor can be written in the crystal oriented coordinate system as:

$$\Delta B(x',y',z') = \begin{vmatrix} p_{11}\varepsilon_1 + p_{12}(\varepsilon_2+\varepsilon_3) & p_{44}\varepsilon_6 & p_{44}\varepsilon_5 \\ p_{44}\varepsilon_6 & p_{11}\varepsilon_2 + p_{12}(\varepsilon_1+\varepsilon_3) & p_{44}\varepsilon_4 \\ p_{44}\varepsilon_5 & p_{44}\varepsilon_4 & p_{11}\varepsilon_3 + p_{12}(\varepsilon_1+\varepsilon_2) \end{vmatrix}, \tag{8}$$

where [22,23]:

$$\begin{cases} p_{11} = -0.0290 \\ p_{12} = +0.0091. \\ p_{44} = -0.0615 \end{cases}$$

In our numerical simulations the values of ε_j in (8) are obtained by COSMOS FEM calculations referring to the "crystal oriented" system. After calculating ΔB for each node using Eq. (8), the corresponding values of ΔB are transformed back to the slab coordinate system. Afterwards, the B tensor is diagonalized, in order to get the indicatrix coefficients of Eq. (5). From these coefficients the refractive indices are directly found.

#202559 - $15.00 USD Received 4 Dec 2013; accepted 27 Jan 2014; published 28 Feb 2014

The propagated beam wavefront is thus calculated from the nodal refractive index values and fitted using Zernike polynomials [30].

As it is well known, any wavefront distribution $f(r,\vartheta)$ in the transverse plane can be described in terms of Zernike polinomials:

$$f(r,\vartheta)=\sum_{n=0}^{\infty}\sum_{m=-n}^{n}\left(a_{nm}Z_n^m(r,\vartheta)\right), \tag{9}$$

where the coefficients a_{nm}, giving the magnitude of the different aberrations, can be calculated inverting the previous equation:

$$a_{nm}=\iint_{circle} f(r,\vartheta)Z_n^m(r,\vartheta)\,r\,dr\,d\vartheta. \tag{10}$$

The wavefront focal length is given in our case by the following equation:

$$f\simeq\left(\frac{r_{MAX}^2}{4\cdot a_{20}}\right), \tag{11}$$

where r_{MAX} is the radius of the pumped region and a_{20} is the defocus coefficient.

3. Discussion of the simulation results

3.1 Ring Cooled Geometry

In this paragraph we show the results obtained from our numerical approach for two different cooling geometries, as described in section 2.1. In the first one, called "RCG" (*i.e.* "Ring Cooling Geometry"), the slab is cooled only on a ring shaped surface on the non-pumped side. In the second one, called "FCG" (*i.e.* "Face Cooling Geometry"), the slab is cooled on the whole surface on the non-pumped side.

Table 1. Doping levels of the uniform/structured samples studied in our numerical simulations.

Sample #	Sample name	Yb percentage in different layers (%)				
		L5	L4	L3	L2	L1
1	*Uniform*	5	5	5	5	5
2	*Graded A*	7	5	5	3	3
3	*Graded B*	7	7	5	3	1
4	*Stepped*	10	10	10	0	0
5	*Capped*	0	10	10	10	0

Each geometry has been analyzed considering 5 different Yb doping distributions, as shown in Table 1, where the first doping value (L1) refers to the layer on the pumped side of the sample, whereas the last one (L5) refers to the layer on the cooled side. They are shown in a reverse order in Table 1, so as to mimic the pumping direction as in Figs. 1(a) and 1(b).

Figure 2 shows the thermal distributions on an *r-z* section of the cylindrical slabs obtained from our simulations for the five samples defined in Table 1. In the mentioned figure, cooled sides are on the left and pumped sides are on the right.

The isothermal surfaces show that, given the ring shaped cooling surface, heat flows out of the pumped volume in a substantially radial way. We can also see that, due to the more uniform pump absorption, graded doping can make the temperature distribution smoother than all the other cases, including the case of uniform doping. Thus also the maximum internal temperature results reduced in this case. However, we will see in what follows that this does not lead to a substantial reduction of the thermal lens. In fact the z-oriented beam propagation determines an averaging of the refractive index variations cancelling the effect of a more uniform pump power absorption.

#202559 - $15.00 USD Received 4 Dec 2013; accepted 27 Jan 2014; published 28 Feb 2014

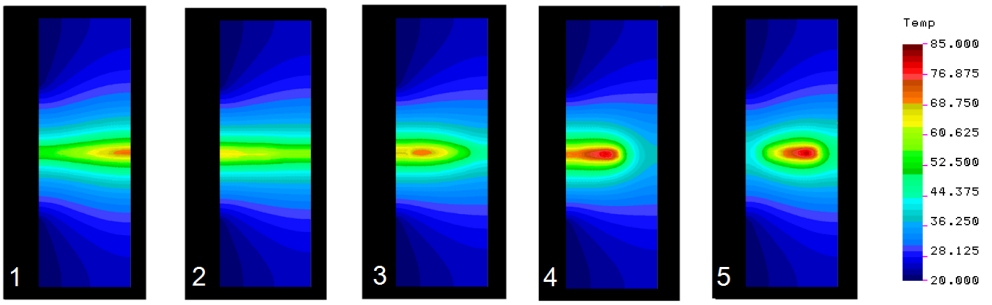

Fig. 2. Temperature distribution in an axial cross-section for the 5 cases in RCG. Maximum temperatures are for the five samples Tmax(1) = 71°C, Tmax(2) = 65°C, Tmax(3) = 71°C, Tmax(4) = 81°C, Tmax(5) = 81°C.

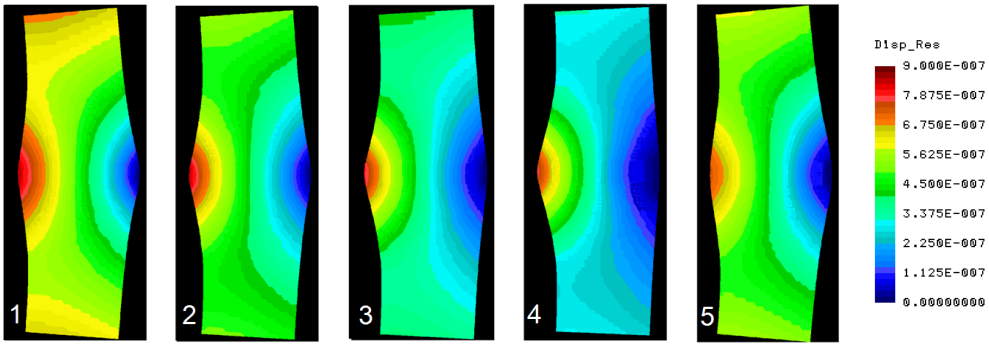

Fig. 3. Surface deformation in an axial cross-section for the 5 cases in RCG.

Figure 3 shows the slab deformations in the 5 analyzed cases. Here it is clear that smaller surface deformations are obtained when there is a low doping level close to the external surfaces. The surface deformations for the five cases are listed in Table 2.

Table 2. Maximum temperature, maximum surface deformations and maximum Von Mises stresses for the 5 analyzed cases in RCG.

Sample #	Max. Temp. [°C]	ΔL_p (pump side) [x10^{-8} m]	ΔL_c (cooler side) [x10^{-8} m]	Max. Von Mises stress [x10^{7} N/m^2]
1	71	3.567	1.940	3.1
2	65	2.476	2.980	2.9
3	71	1.295	3.200	3.35
4	81	0.467	3.420	3.7
5	81	1.315	0.720	3.6

Figure 4 shows the Von Mises stress values for the 5 cases analyzed in RCG configuration. Here it is clear that the "stepped" and "capped" cases, that show an advantage in terms of surface deformations, present higher internal stresses. This is due to the fact that a higher doping has been used in the internal layers, in order to reach the same total pump absorption. Thus the graded sample (# 2) is expected to show the highest fracture-limit power absorption, while the stepped sample (# 4) is expected to show the lowest one.

#202559 - $15.00 USD Received 4 Dec 2013; accepted 27 Jan 2014; published 28 Feb 2014

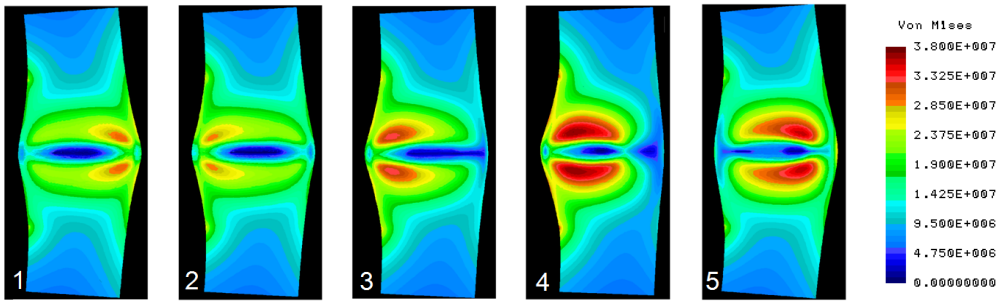

Fig. 4. Von Mises stress distribution in an axial cross-section for the 5 cases in RCG.

In Table 3 the global thermal lens e.f.l.s are given for the 5 sample distributions defined in Table 1, in the RCG case. The maximum focal length deviation from the average value is 3.3%, for this set of samples.

Table 3. Effective focal length (e.f.l.) calculated for the 5 analyzed samples in the RCG configuration (thermal power loading equal to 2.6 W).

Sample #	*e.f.l.* (cm)
1	*8.60*
2	*8.68*
3	*8.87*
4	*8.80*
5	*9.11*

For the sake of a comparison and validation of our modelling, Fig. 5 shows the radial profile of the wavefront obtained with the numerical procedure described in the previous section, compared to the one measured on a real sample using a Shack-Hartman sensor in our lab [24–26].

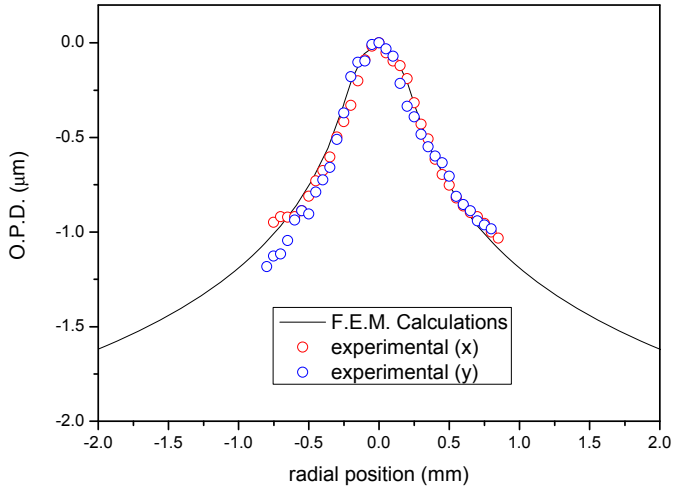

Fig. 5. Comparison of the calculated OPD radial profile and that experimentally measured with a Shack-Hartmann on a 2 mm diameter aperture of our sample, data reported here refer to the uniform doping distribution (sample #1).

The aberrated wave-front is correctly reconstructed both inside and outside the pumped area (0.5 mm diameter). Limiting the aperture to the pumped region the wavefront shape is substantially parabolic (see Fig. 6). This allows us to describe the behaviour of different

#202559 - $15.00 USD Received 4 Dec 2013; accepted 27 Jan 2014; published 28 Feb 2014

samples in terms of thermal lens Dioptric Power. Interestingly the experiments performed on a few selected cases [24] confirm that, in this geometry, the thermal Dioptric Power is substantially independent from the longitudinal doping distribution. This validates our modelling results. A more detailed description of the experimental tests is discussed in a different paper [26], both in terms of thermal lens and in terms of thermally induced depolarization.

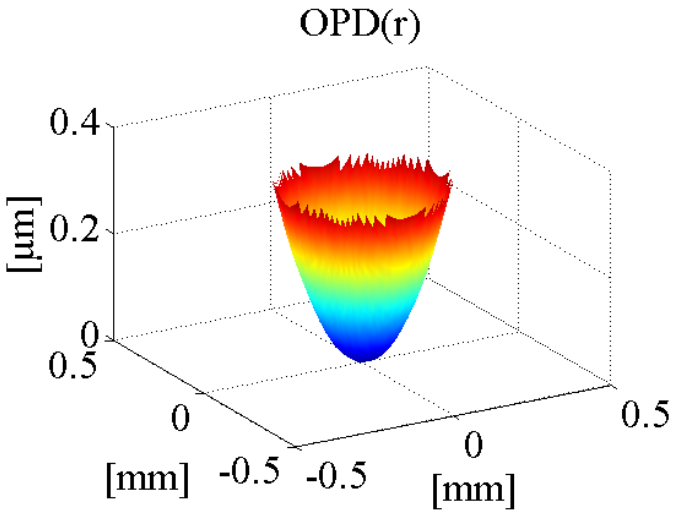

Fig. 6. OPD approximated using Zernike polynomials (sample n.1).

3.2 Face Cooled Geometry

The situation is quite different in the case of a mainly longitudinal heat flow, as exemplified in the FCG configuration of our analysis.

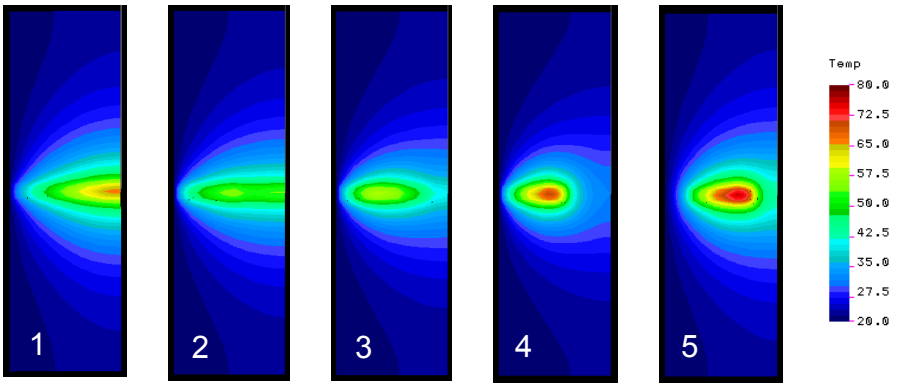

Fig. 7. Temperature distribution in an axial cross-section for the 5 doping cases of Table 1, adopting a Face Cooling Geometry (FCG) with 3 mm thickness and 0.5 mm pump volume diameter.

Figure 7 shows the temperature distribution on axial sections (*r-z*) in FCG configuration referring to the same 5 samples studied in the RCG case. Here we can observe that the heat flux is no longer purely radial, as in RCG configuration, but it shows a relevant longitudinal component. Of course the relative relevance of the longitudinal flux is higher for systems with higher aspect-ratios d/t, where d is the pumped volume base diameter and t the sample thickness. Thus we have analyzed the thermal lens behaviour for the five sample doping distributions in the FCG configuration for different aspect ratios. Diameters and thicknesses

#202559 - $15.00 USD Received 4 Dec 2013; accepted 27 Jan 2014; published 28 Feb 2014

have been chosen in such a way as to maintain the same pumping power densities in all cases (*i.e.* scaling the square root of the pumping volume diameter with the inverse of the thickness). Figure 8 summarizes the results of our analysis in terms of thermal lens Dioptric Power. Our numerical simulations allow to evaluate the different contributions to the thermal lens effect described in Eq. (1), namely direct thermal refractive index dependence, photo-elastic contribution and surface deformations. In Fig. 8 the three contributions to the Dioptric Power are separately indicated.

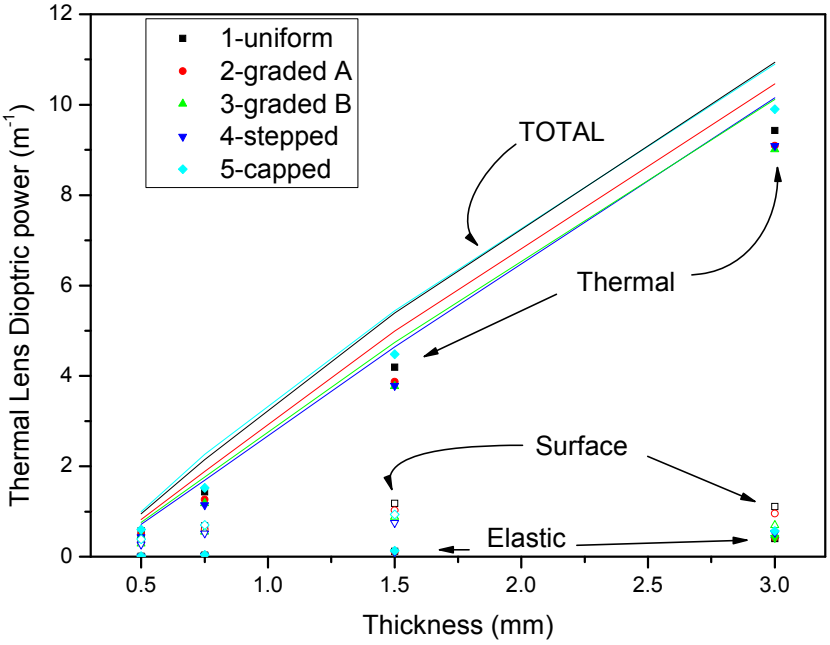

Fig. 8. Thermal lens Dioptric Power versus thickness for the five analyzed doping distributions in case of Face Cooling Geometry.

The relative weight to the total thermal lens in the analyzed cases is reported in Table 4. The table shows the minimum and maximum share of each type of effect.

Table 4. Minimum and maximum relative contributions to the thermal lens Dioptric Power.

Cooling	Thickness [mm]	Thermal [%]	Surface [%]	Elastic [%]
RCG	3.0	84 – 88	5 – 12	3.6 - 6.8
FCG	3.0	86 – 91	5 – 10	3.6 - 5.3
FCG	1.5	75 – 80	19 – 22	3.1 - 3.4
FCG	0.75	66 – 68	30 – 32	1.7 - 1.9
FCG	0.5	60 - 61	38 - 39	1.0 - 1.1

Some important considerations can be drawn from this analysis. First of all one can see that the maximum relative focal length deviation from the average value grows from 4% in the case of 3 mm thick samples to 18% in the case of 0.5 mm thick samples. This fact confirms that varying the doping distribution results in a more significant outcome in systems with a strongly longitudinal heat flux. Moreover it can be noted that the thermal and elastic contributions to the thermal lens dioptric power scale linearly with the thickness while the

#202559 - $15.00 USD Received 4 Dec 2013; accepted 27 Jan 2014; published 28 Feb 2014

surface contribution does not. Thus the relative importance of the different contributions changes with the aspect-ratio as clearly evidenced in Table 4.

In general the lowest direct thermal effect is obtained when maximizing the doping close to the cooling surface. The lowest photo-elastic effect is obtained in systems with less steep doping gradients. Finally, smaller surface deformations are obtained in systems with small doping close to the external faces.

4. Conclusions

In this paper we have reported on a numerical simulation procedure suited to analyze the thermo-mechanical behaviour of Yb:YAG ceramic slabs with longitudinal doping gradient, along with the corresponding optical effects. Our work was motivated by the availability of structured slabs with longitudinal doping gradient given by the ceramic sintering technology.

The first set of simulations confirms our experimental observations. They show that a longitudinally structured material is ineffective for the reduction of thermal effects in end-pumped systems with radial cooling. On the contrary longitudinal doping gradients are useful in case of a parallel cooling geometry, such as in the case of disk or active-mirror lasers. This effect is more pronounced in high aspect-ratio systems.

Our numerical simulations also allow to evaluate the relevance of the different contributions to the thermal lens effect, namely direct thermal refractive index dependence, photo-elastic contribution and surface deformations. The future steps will be the study of specific laser designs, seeking ways to optimize the pump energy deposition profile in order to achieve a better thermal management and a mitigation of deleterious optical effects. The final aim is the scaling of DPSSLs based on ceramic doping gradient media to higher peak and average powers.

Acknowledgments

We acknowledge support from the EC initiative “LASERLAB-EUROPE” (EC contract no. 284464) - Joint Research Activity WP33 - “European Research Objectives on Lasers for Industry, Technology and Energy (EURO-LITE)” and the HiPER (ESFRI-FP7) project. J.H. would also like to acknowledge the financial support from a specific university research grant (MSMT No 20/2013); P.F would also like to acknowledge the financial support from regione Toscana through the project “R&D of innovative wavefront sensors and Adaptive Optics for laser-driven Radiological Devices – AdOpRad” (protocollo ISTI-CNR No 0000745, 09/03/2012).